Testing and modeling of the viscoplastic and fracture behavior of metallic foils used in lithium-ion batteries

by

Colin Bonatti

Ingénieur diplômé de l'École Polytechnique (2013)

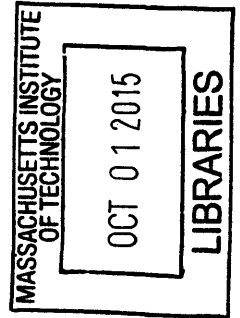Submitted to the Department of Mechanical Engineering in partial fulfillment of the requirements for the degree of

Master of Science in Mechanical Engineering

at the

MASSACHUSETTS INSTITUTE OF TECHNOLOGY

September 2015

Signature redacted

Author.................................

Colin Bonatti
Department of Mechanical Engineering
August 10, 2015

Signature redacted

Certified by...............   ....

Tomasz Wierzbicki
Professor of Applied Mechanics
Thesis Supervisor

Signature redacted

Accepted by..........................

David E. Hardt
Professor of Mechanical Engineering
Chairman, Graduate Committee
Department of Mechanical Engineering

Testing and modeling of the viscoplastic and fracture behavior of metallic foils used in lithium-ion batteries

by

Colin Bonatti

Abstract

Aluminum 1235-H18 foils with sub-micron grain dimensions are often used as current collectors in Li-ion batteries. Due to their contribution to the structural integrity of batteries under impact loading, their plastic and fracture response is investigated in detail. Using a novel micro-tensile testing device with a piezoelectric actuator, dogbone specimens with a 1.25mm wide and 5.7mm long gage section are tested for three different in-plane material orientations and for strain rates ranging from 10^{-5}/s to 10^{-2}/s. It was found that the stress at a proof strain of 2% increased by about 25% from 160MPa to 200MPa within this range of strain rates. Furthermore, pronounced in-plane anisotropy is observed as reflected by Lankford ratios variations from 0.2 to 1.5. A material model is proposed which borrows elements of the anisotropic Yld2000-2d plasticity model and integrates these into a basic viscoplasticity framework that assumes the multiplicative decomposition of the equivalent stress into a strain and strain rate dependent contributions. The anisotropic fracture response is characterized for a strain rate of 10^{-3}/s using notched tension and Hasek punch experiments. It is found that a simple stress-state independent version of the anisotropic MMC fracture initiation model provides a reasonable approximation of the observed experimental results.

3

4

Acknowledgements

6

Table of Contents

8

1. Introduction

Standard commercial rechargeable lithium-ion batteries are composed of a negative graphite electrode (anode) and a positive metal oxide electrode (cathode). Prominent examples for the latter are lithium cobalt oxide, lithium manganese oxide and lithium iron phosphate. Metallic foils commonly serve as substrate for the electrode materials and as current collectors, with aluminum foil being the industry's prime choice for the cathode substrate. Substrate foils also account for an important part of the structural strength of a battery (see Mikolajczak et al., 2011). In particular, they play a major role when the battery is subject to accidental impact loading. The anode and cathode layers as well as the so-called separator layer have only little structural resistance. A short circuit followed by thermal run-away happens when the (polymer) separator fails, creating direct contact between the conducting electrodes. The metallic foils used in batteries typically have very low ductility and are prone to fail during mechanical loading.

In the context of optimizing the structural safety of battery systems, the deformation response of foils must be characterized and modeled. The main scientific challenges associated with this undertaking are the high anisotropy induced by severe cold rolling and the potentially high rate sensitivity as reported by others for polycrystalline materials with submicron grain sizes (e.g. Wei 2007). After Hill's (1948) pioneering work on the formulation of quadratic anisotropic yield functions, numerous anisotropic yield functions have been developed based on non-quadratic isotropic criteria (Hershey (1954), Hosford (1972)) through the linear transformation of the stress tensor argument (Barlat et al. (2003), Karafillis and Boyce (1993), Bron and Besson (2004)). The works of Aretz et al. (2007), Korkolis and Kyriakides (2008) and Dunand et al. (2012) provide examples for the successful validation of the so-called Yld2000-2d anisotropic plasticity model (Barlat et al., 2003) for aluminum based on multi-axial experiments.

May et al. (2005) compared the strain rate sensitivity of conventional and ultrafine-grained pure aluminum under compression. Quantifying the strain rate sensitivity through the strain rate exponent $m = \partial \ln \sigma / \partial \ln \dot{\varepsilon}$ based on measurements performed at strain rates ranging from $10^{-5}/s$ to $10^{-3}/s$, they reported a nearly four-fold higher strain rate sensitivity for the ultra-fine grained material (grain size of less than $500nm$) at room

9

temperature. Dao et al. (2008) investigated the tensile response of copper for grain sizes ranging from $10nm$ to $100\mu m$. From experiments performed at strain rates between about $10^{-4}/s$ and $10^{-1}/s$, they found that the strain rate sensitivity increases dramatically from about $m = 0.006$ for grain sizes larger than $1\mu m$ to up to $m = 0.06$ for ultra-fine grained microstructures. The model by Y. Wei et al. (2008) explains the initial grain-size dependent strain-rate sensitivity in polycrystals through a mechanism transition from grain boundary sliding- and diffusion-dominated creep to grain interior plasticity-dominated flow. More details on analytical models describing the mechanism responsible for the strain rate effects in ultrafine grain polycrystals can be found in the review by Q. Wei (2007).

Given the high strain rate sensitivity of fine grained materials, rate-dependent plasticity or viscoplasticity models need to be employed to describe their stress-strain response – even at room temperature and low strain rates. Different from viscoplasticity models, rate-dependent plasticity formulations postulate the existence of a purely elastic domain. For conventional coarse grain materials at room temperature, the Johnson-Cook type of rate-dependent plasticity models are widely used to describe their increased strain rate sensitivity at high strain rates (e.g. Johnson and Cook (1982), Roth and Mohr (2014)). Viscoplastic formulations are more popular when conventional coarse grained metals are subject to low and intermediate strain rates at elevated temperatures (see review by Lin and Chen (2011)). The characteristic ingredient of viscoplastic constitutive equations is the so-called viscosity function or viscoplastic potential (see review by Chaboche (2008)) which describes the relationship between a scalar stress measure and the equivalent plastic strain rate. Basic functions assume the equivalent plastic strain rate to be a power-law or hyperbolic sine function of the equivalent stress (e.g. Garofalo (1963)). In the context of hot working of metals, Jonas et al. (1969) and Brown et al. (1989) proposed a combined power/hyperbolic functional dependence to provide an accurate description of the viscoplastic response of BCC and FCC materials.

Aside from modeling challenges that stem from the submicron grain size in cold-rolled cathode foils, there are substantial experimental challenges associated with the micro-tensile testing of thin foil materials. Several experimental procedures for the tensile testing of a few microns thick or thinner polycrystalline materials have been developed for thin

10

metallic films used in micro-electronic and micro-mechanical devices. For example, Espinosa et al. (2003) came up with a membrane deflection technique, where a nanoindenter tip applies an out-of-plane load onto a free-standing film double-dogbone specimen to generate tension in the specimen gage sections. Xiang et al. (2005) developed a plane-strain bulge test for thin films. For a $2.8\,\mu m$ thick Cu film, the free-standing area subject to water pressure loading was $2.5 \times 10mm^2$. However, as discussed in Pardoen et al. (2010), it is difficult to extract fracture strains from plane strain bulge test due to heterogeneous strain fields near the specimen boundaries. Bending-free direct tension testing techniques for thin films have also been developed (e.g. Haque and Saif (2003), Zhu and Espinosa (2005), de Boer et al. (2008), Gravier et al. (2009)) and it is today feasible to perform ductile fracture experiments on thin films for a wide range of stress states by varying the specimen shape (e.g. Pardoen et al. (2010)). As an alternative to using a multi-strain gage load cell, the applied forces are estimated based on elastic strain measurements on either the specimen shoulders or the micro-actuator.

For foil testing, the specimen cutting, handling and clamping poses another main challenge in addition to applying small displacement increments and measuring low forces. In the case of thin film specimens deposited onto Si wafers (e.g. through electroplating or sputtering), the substrate provides an excellent support during specimen handling. Even after partial removal of the wafer for free-standing gage sections, the specimen shoulders call still remain on the substrate material to facilitate handling (e.g. Leisen et al. (2015)). Additionally the shape of such film specimens can already be defined during manufacturing through lithography (Andre et al., 2007). Obtaining specimens from rolled foil stock usually requires additional machining to obtain the desired in-plane shape. Gudlavalleti et al. (2006) designed a flexure-based testing machine with an integrated piezoelectric motor. They extracted $1mm$ wide and $7mm$ long miniaturized dogbone specimens from $16\,\mu m$ thick aluminum foil through shear cutting with a custom-made sharp die and employed mechanical clamps to attach the specimen to the testing machine. Kim and Huh (2011) extracted micro-tensile specimen with a $0.2mm$ wide and $1mm$ long gage section from $0.1mm$ thick Cu foil through photo etching. As Gudlavalleti et al. (2006), they made use of mechanical grips to attach their specimen to a high speed micro tensile testing machine. Kachold et al. (2013) made use of a Nd-YAG solid state laser to cut $1.6mm$ wide

dogbone specimens from about $40\mu m$ thick nanocrystalline diamond foil. For detailed reviews of micro-testing techniques and apparatus at various scales see Hemker and Sharpe (2007) and Gianola and Eberl (2009).

It is the objective of the present work to predict the inelastic deformation response of aluminum alloy 1235-H18 foil, which is used as a current collector in lithium-ion batteries. Experiments at strain rates ranging from 10^{-5}/s to 10^{-2}/s are performed on laser cut specimens using custom-made micro-tension and micro-punch testing devices. Images are continuously acquired during the experiments using optical microscopy. The surface strain fields are subsequently determined through digital image correlation. In addition to the effect of strain rate, special attention is paid to the effect of foil anisotropy on plasticity and fracture initiation, both from an experimental and modeling point of view. A viscoplasticity model is proposed which uses an extension of the Yld2000-2D equivalent stress definition as the viscoplastic flow potential. Furthermore, an anisotropic equivalent plastic strain measure is introduced to predict the onset of fracture initiation.

2. Material and specimens

The material considered is an aluminum alloy 1235 foil in its cold–rolled H18 state. It features a minimum of 99% of aluminum content by weight and is used as a current collector in lithium-ion battery electrodes. It was purchased from MTI Corporation (Richmond, CA) in the form of a 300mm wide coil with a minimum coil radius of 80mm. An average foil thickness of 16μm was determined from optical measurements on anion beam cut cross-section (Fig. 1a). EBSD analysis of the same cross-section revealed an average grain size of 800nm along the thickness direction with a coarser microstructure near the foil surfaces and submicron sized grains within the central region (see upper right insert in Fig. 1a). Selected pole figures (Fig. 1b) show the cold rolling texture of the FCC foil material.

Figure 2 provides an overview of all specimens employed in this work:

(1)   Uniaxial tension (UT) specimen: a miniaturized (by factor 10) ASTM E345-93 Type A dogbone specimen for uniaxial tension with a gage section width of 1.25mm and a uniform length of 5.7mm;

(2)   Notched tension (NT) specimens with a minimum gage section width of 1mm and different notch radii: $R=0.67mm$ (NT06), $R=1mm$ (NT1), and $R=2mm$ (NT2).

(3)   Hasek (HS) specimen for out-of-plane punch loading with a minimum gage section width of 2mm and a shallow notch radius of $R=11mm$.

All specimens are extracted from the foil using a CNC Nd-YAG solid state laser with a wave length of 1064nm (Electrox Scorpion Rapide). Due to the nature of the cutting procedure (which involves local melting), the cutting process modifies the material microstructure within a zone of approximately 25μm width (Fig 1c).

It is worth noting that the overall dimensions of the tensile specimens provide enough structural stiffness for specimens to withstand their own weight (when considered as a cantilever beam). In other words, the specimens can be handled using tweezers while remaining flat (no wrinkling or buckling) even without any in-plane tensile load applied. In view of characterizing the effect of in-plane anisotropy, the tensile specimens have been

extracted along three different material directions, i.e. the angle between the principal loading axis and the foil rolling direction was either 0° (rolling direction, RD), 45° (diagonal direction, DD) or 90° (transverse direction, TD).
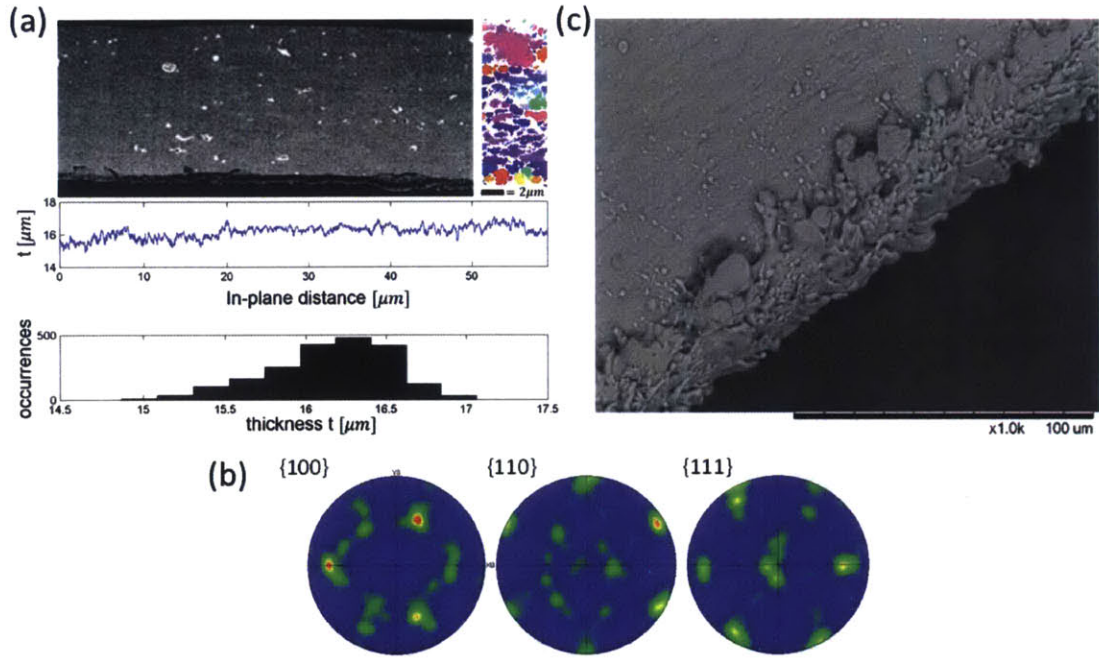

Figure 1. (a) Ion beam polished cross-section with EBSD and thickness distribution; (b) in-plane pole figures of selected crystal planes, (c) top view of laser cut edge.
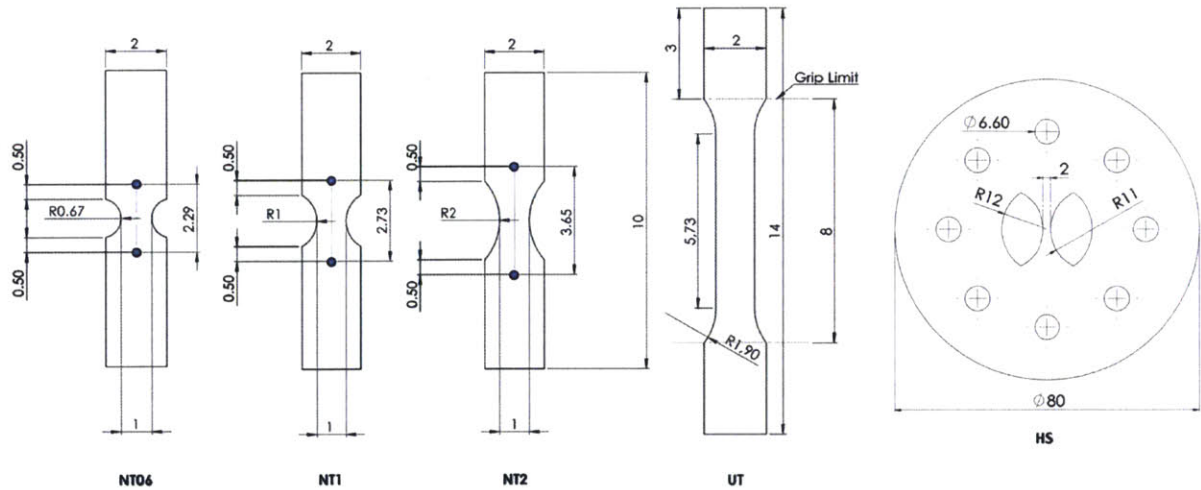

Figure 2. Specimen geometries.

3. Experimental procedures

The above specimens are tested under monotonic loading conditions all the way to fracture using a micro-tensile testing device and a micro-punch testing device.

3.1.Micro-tensile testing device

Figure 3 shows a photograph of the micro-tensile testing device that was developed for this study. Its main components are:

(1) Piezo electric micro-legs linear motor (Model LEGS Linear Twin 20N, Micromo, Clearwater FL) with a maximum speed of up to $10mm/s$ and a displacement step of less than $1nm$; the motor (part ①) comes with a $4mm$ wide and $3mm$ thick drive rod.

(2) A single point load cell (Model LCAE-2KG, Omega, New York NY) which is rated for loads of up to 20N (part ②).

Both components are mounted onto a non-magnetic aluminum frame (part ③). A small aluminum grip (see part ④ in detail) is screwed onto the drive rod featuring a flat $2mm$ wide and $5mm$ long bonding area which is parallel to the specimen midplane. The same type of grip (part ⑤) is attached to the load cell. After aligning both grips and adjusting the initial drive position to the total specimen length, the specimens are glued onto the bonding area of the grips. Optimal results in terms of assembly time, squeeze-out and bond strength have been achieved using a strain gage adhesive (M-Bond 200, Micro-Measurements), which allows for alignment corrections before curing. The width of the gripping area matched that of the specimen shoulders to facilitate the specimen alignment.

The time, actuator displacement (as estimated from the known micro-step size) and force were recorded via the analog signal acquisition software AGNES (in-house developed Labview software) at frequencies of 2 to 100 Hz, depending on the total duration of the experiment.

15
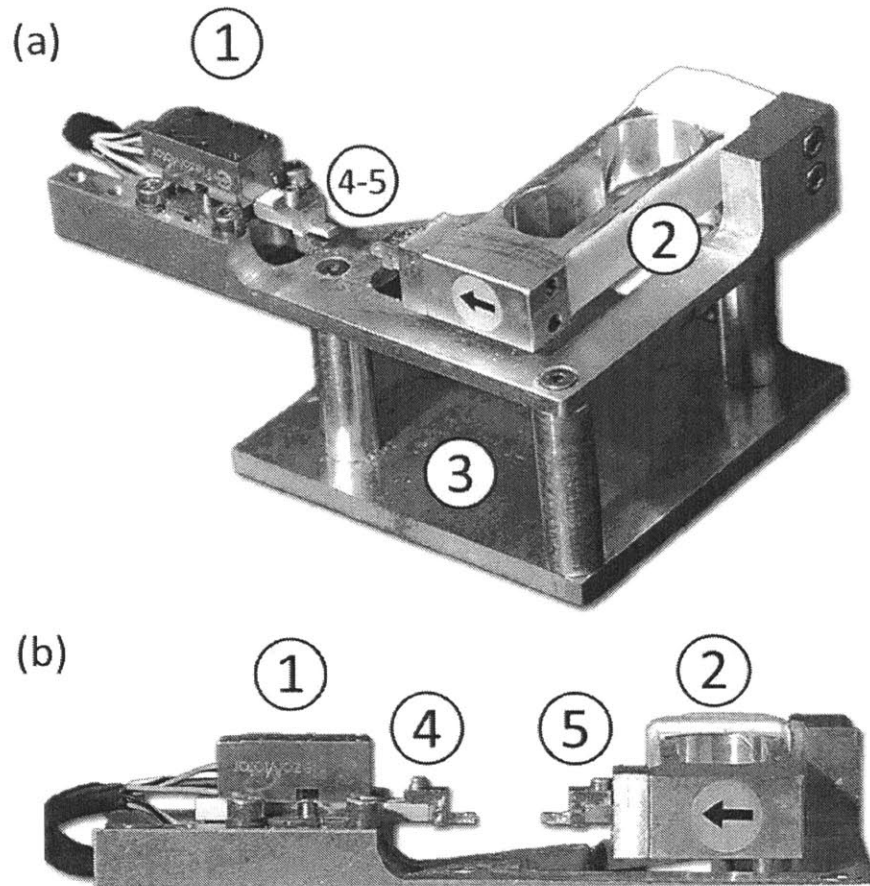
Figure 3. Micro-tensile testing device: (a) 3D view, (b) side view, showing the piezo-legs actuator ①, the 20N load cell ②, the non-magnetic frame ③, and the specimen holding fixtures.

3.2. Micro-punch testing device

A micro-punch testing device (Fig. 4) is used to apply out-of-plane loads onto the disk shaped foil specimens (Fig. 2). The device features a 10mm diameter hemispherical punch and a die with an inner diameter of 24mm with a 30° chamfered edge. The special feature of this custom-made non-magnetic device is that the punch remains stationary while a servo-mechanical screw drive controls the vertical motion of the die with respect to the punch. This configuration facilitates the monitoring of the specimen surface during the experiment and eliminates the need for stereo systems for apex surface strain measurements. The specimen is clamped through a blank holder with eight M6 hexagonal cap screws.

16
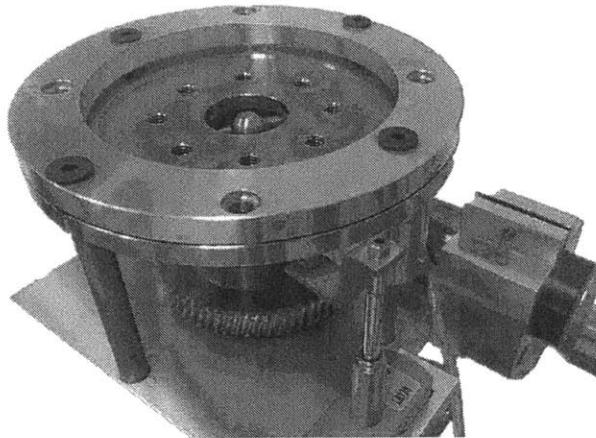
Figure 4. Mini-punch testing device.

3.3. Displacement and strain measurements

The displacement fields and strain fields are determined using planar Digital Image Correlation (DIC). After mounting the specimen, the respective micro testing device is therefore positioned below an optical microscope (Model Stemi SV11, Zeiss). Depending on the specimen type, different magnification settings were employed and different speckle patterns were applied using black ink in conjunction with an air brush (see Berfield et al. (2010) for details):

1) Uniaxial tension: the average speckle size was about $80\mu m$ and has been monitored at a resolution of $9\mu m$ per pixel. The main purpose of the DIC measurements on the UT specimens was to serve as optical extensometer for average axial and width strain measurements.

2) Notched tension: a smaller average speckle size of only $20\mu m$ is applied to compute the strain fields within the gage section. Here, a resolution of $3\mu m$ per pixel has been chosen.

3) Hasek punch: the application of a speckle pattern has been omitted as the natural surface pattern turned out to be sufficiently heterogeneous for digital image correlation. The images were acquired at a resolution of $2\mu m$ per pixel.

17

The application of a uniform white paint layer has been omitted to avoid any influence of paint on the mechanical response of the foil specimens. Deformation-induced brightness variations related to the high reflectivity of the aluminum surface were therefore inevitable. In the absence of an applied speckle pattern, incremental frame-to-frame correlation was thus chosen instead of systematic correlation with respect to the initial configuration. The digital image correlation software VIC 2D (Correlated Solutions, Columbia SC) has been employed with a subset size of 21 pixels and a step size of 5 pixels. Based on the spatial gradient in the surface displacement fields, the logarithmic strain fields have been determined.

Geometry:	UT	NT06	NT1	NT2
Crosshead Velocity$[mm.s^{-1}]$:	1.0×10^{-3}	3.3×10^{-5}	2.5×10^{-5}	2.2×10^{-5}

Table 1. Crosshead velocities for tension experiments at reference strain rate.

4. Experimental results

The experimental program is designed to characterize the large deformation response of aluminum foil 1235-H18. It involves uniaxial tension experiments at different strain rates and along different in-plane directions. In addition, notched tension and Hasek punch experiments are performed.

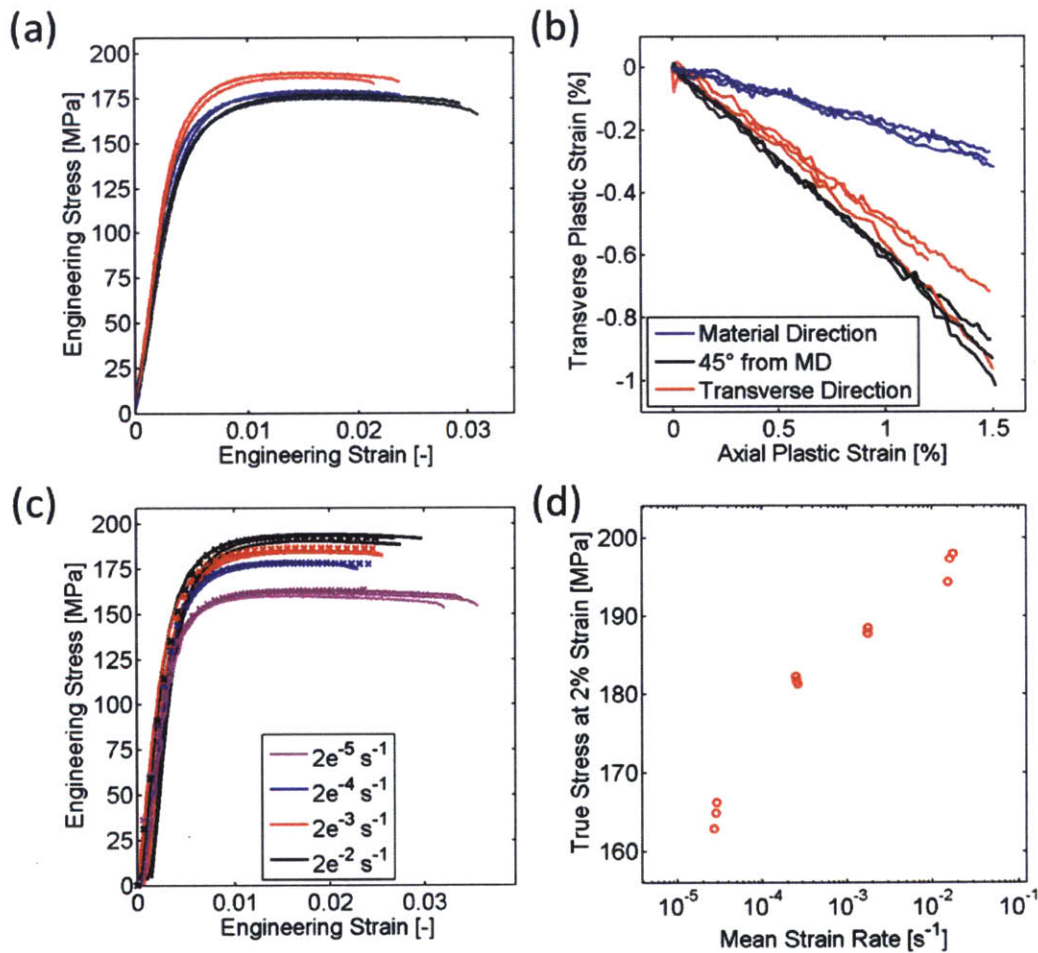**Figure 5. Experimental results for uniaxial tension: (a) engineering stress-strain curve for different specimen orientations at a strain rate of about $1.8 \times 10^{-4}/s$, (b) corresponding width strain measurements, (c) stress-strain curve for rolling direction for different strain rates with experiments as lines and simulations as dots, and (d) yield stress at 2% strain as a function of the strain rate.**

4.1. Uniaxial tension

A first series of uniaxial tension experiments is performed at a constant actuator speed of 1 $\mu m/s$ which equates to a strain rate of about $2 \times 10^{-4}/s$ within the gage section. After determining the axial strain using a $2mm$ long DIC extensometer placed across the crack, and applying standard formulas, the true stress versus logarithmic strain curves are determined. Strains along the width of specimens were estimated over a length of $0.8mm$ at the crack location. Figure 5a summarizes the results from tension experiments along three different material directions. The stress level for tension along the transverse direction (red curves) is about 10% higher than that for the rolling and diagonal directions (blue and black curves, respectively). Fracture occurred at an engineering strain (spatial average along the virtual extensometer length) of 0.023, 0.023 and 0.028 for the transverse, rolling and diagonal directions, respectively. Assuming isotropic elastic behavior, we calculated the inelastic strains along the width and longitudinal specimen directions (Fig. 5b). Furthermore assuming plastic incompressibility, we also determined Lankford ratios from the average slope of the plastic width strain versus plastic thickness strain curve. The obtained respective Lankford ratios for uniaxial tension along the rolling, diagonal and transverse direction are 0.2, 1.5 and 1.1 which indicates a very pronounced in-plane anisotropy.

In addition to the experiments at a strain rate of about $2 \times 10^{-4}/s$, a second series of experiments is performed on RD specimens at higher and lower strain rates: $2 \times 10^{-2}/s$, $2 \times 10^{-3}/s$, and $2 \times 10^{-5}/s$. Note that due to the low ductility of the foil material, the total duration of the very low strain rate experiment ($2 \times 10^{-5}/s$) was still of the order of 30 minutes. The measured stress-strain curves are shown in Fig. 5c. DIC was used to verify the strain rates. The curves are in hierarchical order with respect to the strain rate, i.e. the higher the strain rate the higher the stress level at a given strain. To highlight this effect further, we also plotted the stress at plastic strain of 0.2% as a function of the strain rate. A linear fit of the relationship between the stress and the strain rate yields a strain rate sensitivity factor of $m \approx 0.027$. The Lankford ratios did not vary significantly with the strain rate. As far as the engineering fracture strains are concerned (average over an

20

extensometer length of $2mm$), we observe a decrease in ductility from $2 \times 10^{-5}/s$ to $2 \times 10^{-4}/s$, and an increase for strain rates above $2 \times 10^{-4}/s$.

(a)

(b)

(c)

(d)
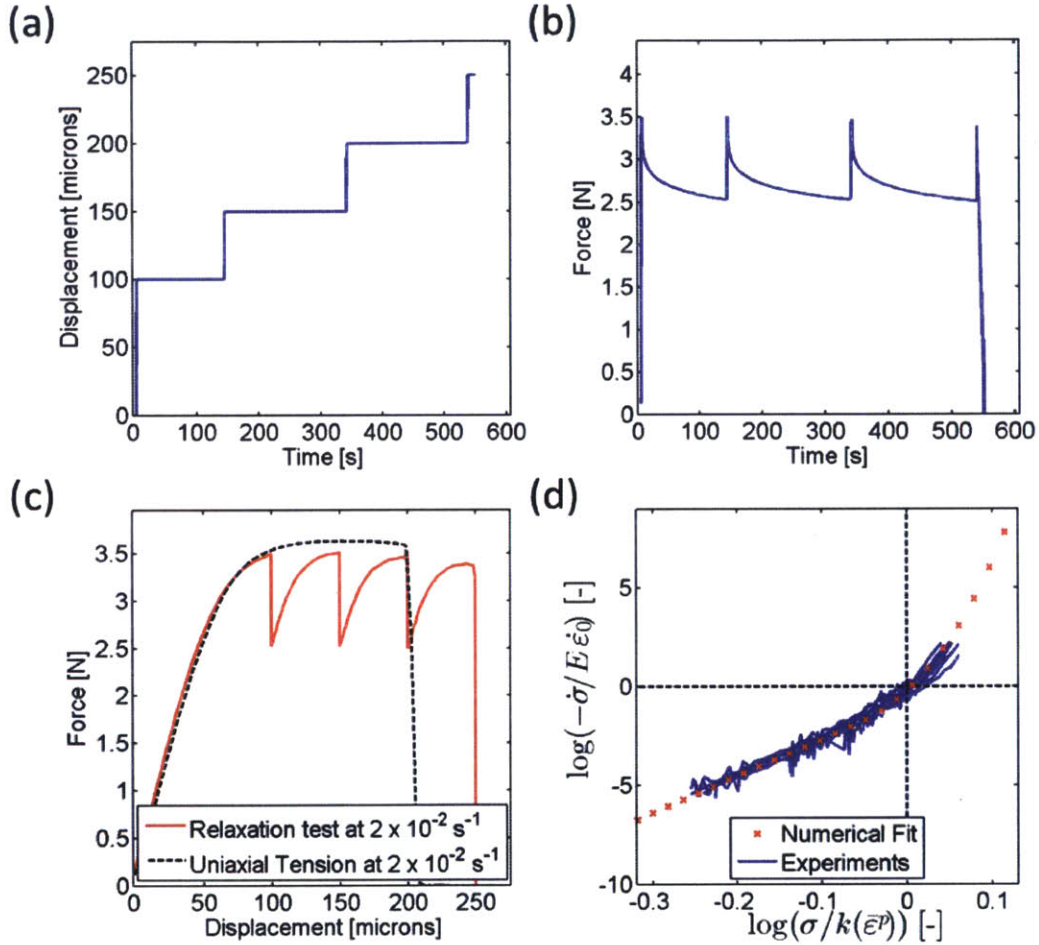
Figure 6. Relaxation experiment: (a) Prescribed displacement history, (b) measured force history, (c) force-displacement curve, (d) Stress-rate as a function of stress during relaxation phases.

4.2. Incremental relaxation experiment

To gain further insight into the time dependent behavior of the aluminum foil, we also performed incremental relaxation experiments on UT specimens parallel to the rolling direction. All loading steps are applied at an actuator velocity of $100 \mu m/s$ which corresponds to a strain rate of approximately $2 \times 10^{-2}/s$ (fastest experiment). In a first

step, a displacement of $100\mu m$ is applied to load the specimen well into the plastic range, to a force of about 3.5N. Subsequently, the actuator position is locked and the specimen left to relax down to a force of about 2.5N. The procedure is repeated with displacement increments of $50 \mu m$ until fracture of the specimen. Figure 6 provides an overview on the recorded signals, including the displacement history (Fig. 6a), the force history (Fig. 6b) and the force-displacement curve (Fig. 6c) along with the result for monotonic loading. The relaxation behavior is better characterized by representing the rate of change of the axial stress, $d\sigma / dt$ as a function of the axial stress, which is presented in Fig. 6d. Observe that all relaxation branches lie approximately on top of each other in this space.
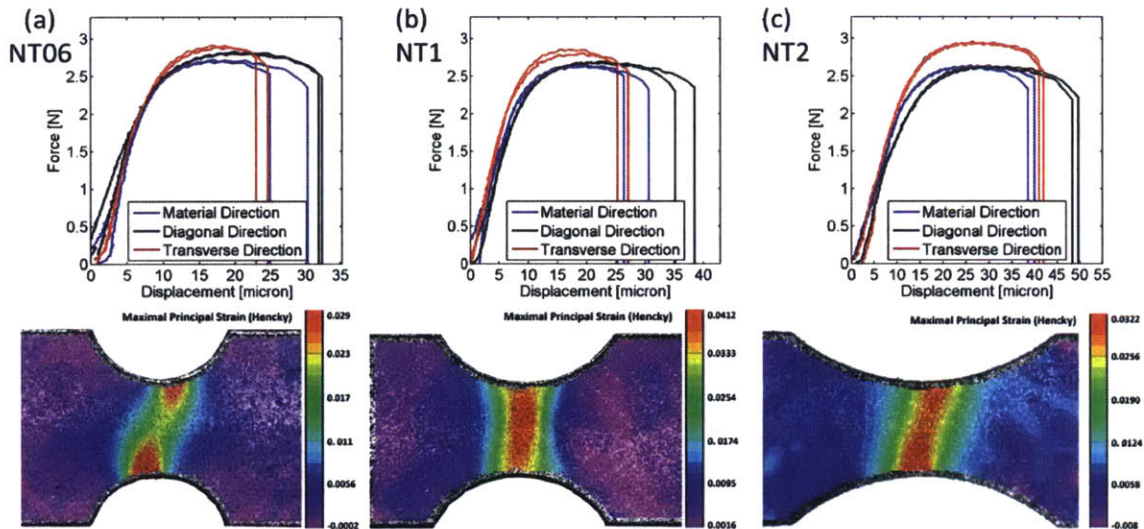
Figure 7. Results for notched tension on specimens of different orientations and different notch radii: (a) R=0.67 mm, (b) R=1mm, (c) R=2mm.

4.3. Notched tension experiments

A full testing matrix of notched tension experiments is executed for three different specimen orientations and three different notch radii. With two repetitions per experiment, a total of 18 notched tension experiments is performed. From an experimental point of view, the notched tension experiments are far more challenging than uniaxial tension since the applied displacement to fracture is about 10 times smaller. Preliminary finite element simulations were performed to determine the correspondence between actuator velocity

22

and strain rate at the center of the specimen for each geometry. Actuator velocities of the order of $0.03\mu m/s$ (see Tab. 1 for exact values) were chosen to ensure a strain rate at the specimen center of approximately $2 \times 10^{-4}/s$. The notched specimens fracture typically at displacements of about $25\mu m$, and the experiments typically lasted around $20min$.
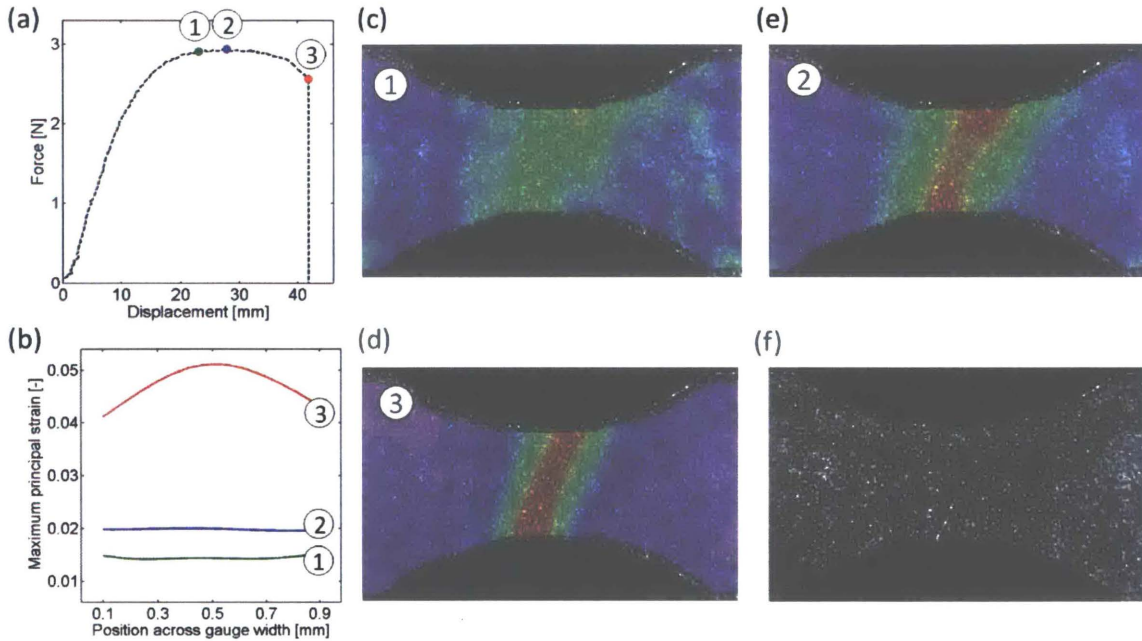
Figure 8. (c)-(e) Evolution of the maximum principal surface strain filed during a notched tension experiment (NT2) along the transverse direction; (a) corresponding force-displacement curve; (b) strain profiles at the specimen center; and (f) fractured specimen.

Figure 7a shows the measured force-displacement response of the NT2 specimens. The displacement is reported for a virtual extensometer length of $3.65mm$ (see also blue dots in Fig. 2b).As for the uniaxial tension specimens, we observe the highest force level for the TD specimens and the highest displacement to fracture for the DD specimens. Note that the force-displacement curves exhibit a maximum followed by a decreasing branch. The detailed evolution of the surface strain fields (maximum principal strain) is shown in Fig. 8 for an NT2 specimen loaded along the transverse direction. Until the force maximum, the highest principal strains prevail near the free edges of the gage section. They reach values of 0.02 at force maximum. After that point, the location of the maximum principal strain gradually shifts towards the center of the specimen.

The results for all other specimens are very similar, as far as the ordering of the results with respect to the specimen orientation is concerned. The main difference is that the overall displacement to fracture decreases with increasing notch acuity. A force increase with notch acuity for the DD, as well as a more pronounced decrease in displacement to fracture (as compared to the other two orientations) for the TD, are also observed. At the instant of fracture, the maximum principal strains are found to be on average of 0.065, 0.075 and 0.054 for the RD, DD and TD specimens, respectively.

(a)   (b)
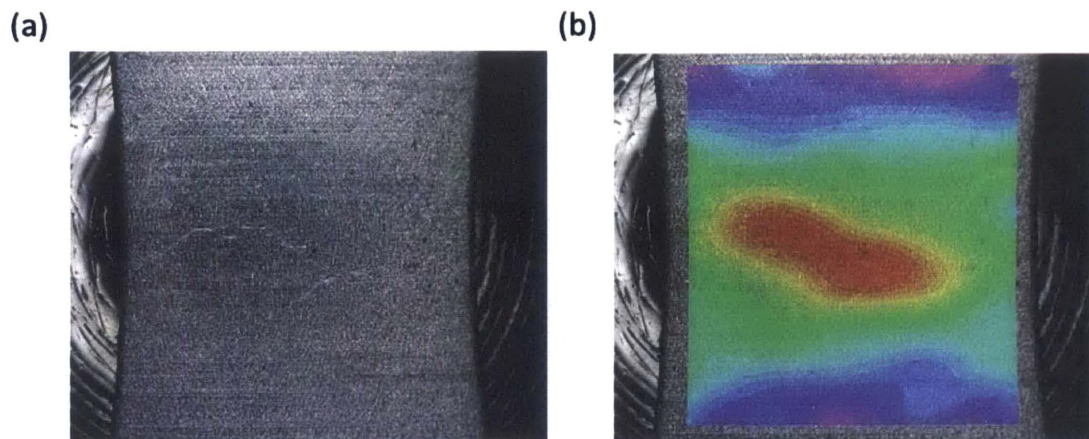
Figure 9. Hasek punch experiments: (a) cracks visible on specimen surface, (b) maximum principal logarithmic surface strain field at the instant of fracture initiation.

4.4. Punch experiments

The punch experiments are performed at a constant velocity of $3\mu m/s$. The force-displacement curve is not reported here for punch experiments as our interest is limited to determining the fracture strains on the specimen surface (and the load cell sensitivity was not adjusted to our purposes). Additional experiments on specimens without any cutouts failed prematurely near the blank holder boundaries and the results are thus not explored further. The results for the Hasek specimen geometry on the other hand are of good quality: as the microcracks in Fig. 9a demonstrate, fracture initiated near the specimen center, away from the lasercut specimen boundaries. Failure occurred following a consistent pattern for each of the loading directions. Specimens loaded along the RD and the TD failed by developing $100\mu m$ long cracks transverse to the loading directions, before propagating

24

diagonally. Specimens loaded in the DD failed by developing a straight crack through the whole gage section, oriented along the TD. Simulations (discussed in paragraph 6.2) revealed that an equivalent plastic strain rate of $1.4 \times 10^{-3}/s$ was reached in average in a Hasek specimen.

Remark: Inspired by the basic fracture testing program for sheet metal proposed by Dunand and Mohr (2010), an attempt was also made to perform experiments on micro-tension specimens with a central hole. However, the results could not be explored due to the buckling of the regions right above and below the central hole. In theory, this problem could be overcome by decreasing the in-plane specimen dimensions further, thereby increasing the specimen's local bending stiffness with respect to the compression stresses. This option was not explored here. Aside from changing the load cell, a time-consuming FIB preparation of the specimen edges would be required to keep the machining effected zone near the specimen boundaries small as compared to the characteristic specimen in-plane dimensions.

5. Anisotropic viscoplasticity and fracture model

5.1. Viscoplasticity model

5.1.1 General mathematical form

A new viscoplasticity model is proposed which borrows elements of the anisotropic plasticity model Yld2000-2d of Barlat et al. (2003) and integrates these into a viscoplasticity framework.

The constitutive equation for the Cauchy stress tensor reads

$$\boldsymbol{\sigma} = \mathbf{C} : (\boldsymbol{\varepsilon} - \boldsymbol{\varepsilon}_p) \tag{1}$$

with $\boldsymbol{\varepsilon}$ and $\boldsymbol{\varepsilon}_p$ denoting the total and plastic strain tensors, and the elastic stiffness tensor $\mathbf{C}$. The stress derivative of the equivalent stress $\bar{\sigma} = \bar{\sigma}[\boldsymbol{\sigma}]$ defined by Barlat's Yld2000-2d model is used to prescribe the direction of viscoplastic flow,

$$\dot{\boldsymbol{\varepsilon}}_p = \dot{\bar{\varepsilon}}_p \frac{\partial \bar{\sigma}}{\partial \boldsymbol{\sigma}}, \tag{2}$$

while the equivalent plastic strain rate $\dot{\bar{\varepsilon}}_p$ is controlled through the viscoplastic constraint

$$\bar{\sigma} = k[\bar{\varepsilon}_p] g[\dot{\bar{\varepsilon}}_p] \tag{3}$$

which is formally rewritten in the form

$$\ln\left[\frac{\bar{\sigma}}{k[\bar{\varepsilon}_p]}\right] = \ln\left[g[\dot{\bar{\varepsilon}}_p]\right] =: f_v\left[\ln\left[\frac{\dot{\bar{\varepsilon}}_p}{\dot{\varepsilon}_o}\right]\right]. \tag{4}$$

In Eq. (4), f_v is the *relative viscosity function* relating the current equivalent stress to the applied plastic strain and the current equivalent plastic strain rate. The reference strain rate $\dot{\varepsilon}_0$ is defined as the strain rate for which $\bar{\sigma} = k[\bar{\varepsilon}_p]$ which implies $f_v[0] = 0$. According to (4), the strain rate sensitivity is $m = f_v{}'$, which is only constant if f_v is a linear function.

26

5.1.2 Definition of the equivalent stress and plastic strain

Given the pronounced anisotropy of the foil material, the equivalent stress definition of the Yld2000-3d model (Dunand et al., 2012) is adopted. It corresponds to the 3D extension of the widely used (and validated) Yld2000-2d model of Barlat et al. (2003). The central idea of the Yld2000 models is to write the equivalent stress in terms of linearly transformed stress tensor (vector) arguments. Denoting the Cauchy stress vector as

$$\vec{\sigma} = \{\sigma_{xx} \quad \sigma_{yy} \quad \sigma_{zz} \quad \sigma_{xy} \quad \sigma_{yz} \quad \sigma_{zx}\}, \tag{5}$$

The transformed stress deviator vectors

$$\vec{s}' = \{s'_{xx} \quad s'_{yy} \quad s'_{xy} \quad s'_{yz} \quad s'_{xz}\} \text{ and } \quad \vec{s}'' = \{s''_{xx} \quad s''_{yy} \quad s''_{xy} \quad s''_{yz} \quad s''_{xz}\}$$

are defined through the linear transformations,

$$\vec{s}' = \mathbf{L}'\vec{\sigma} \text{ and } \quad \vec{s}'' = \mathbf{L}''\vec{\sigma} \tag{6}$$

with

$$\mathbf{L}' = \frac{1}{3}\begin{bmatrix} 2\alpha_1 & -\alpha_1 & -\alpha_1 & 0 & 0 & 0 \\ -\alpha_2 & 2\alpha_2 & -\alpha_2 & 0 & 0 & 0 \\ 0 & 0 & 0 & 3\alpha_7 & 0 & 0 \\ 0 & 0 & 0 & 0 & 3 & 0 \\ 0 & 0 & 0 & 0 & 0 & 3 \end{bmatrix} \tag{7}$$

and

$$\mathbf{L}'' = \frac{1}{9}\begin{bmatrix} -2\alpha_3 + 2\alpha_4 + 8\alpha_5 - 2\alpha_6 & -4\alpha_4 + 4\alpha_6 + \alpha_3 - 4\alpha_5 & \alpha_3 + 2\alpha_4 - 4\alpha_5 - 2\alpha_6 & 0 & 0 & 0 \\ 4\alpha_3 - 4\alpha_4 - 4\alpha_5 + \alpha_6 & -2\alpha_3 + 8\alpha_4 + 2\alpha_5 - 2\alpha_6 & -2\alpha_3 - 4\alpha_4 + 2\alpha_5 + \alpha_6 & 0 & 0 & 0 \\ 0 & 0 & 0 & 9\alpha_8 & 0 & 0 \\ 0 & 0 & 0 & 0 & 9 & 0 \\ 0 & 0 & 0 & 0 & 0 & 9 \end{bmatrix}. \tag{8}$$

Note that the third normal component of the deviatoric transformed stress tensor is given through the vanishing trace condition, i.e.

$$s'_{zz} = -(s'_{xx} + s'_{yy}) \text{ and } \quad s''_{zz} = -(s''_{xx} + s''_{yy}). \tag{9}$$

27

The linear transformations L' and L'' are specified through the eight parameters $\alpha_1,...,\alpha_8$ of the Yld2000-2d model (Barlat et al., 2003). For $\alpha_i = 1$, s' and s'' are equal and define the deviatoric Cauchy stress tensor.

With the transformed stress vectors at hand, the anisotropic equivalent stress is defined as,

$$\bar{\sigma} = \frac{1}{2^{1/a}} \left(\phi'(\mathbf{s}') + \phi''(\mathbf{s}'') \right)^{\frac{1}{a}} .$$ (10)

with

$$\phi'(\mathbf{s}') = \left[(s'_{xx} - s'_{yy})^2 + 4(s'^2_{xy} + s'^2_{xz} + s'^2_{yz}) \right]^{\frac{a}{2}}$$ (11)

and

$$\phi''(\mathbf{s}'') = \left[\frac{3}{2}(s''_{xx} - s''_{yy}) + \frac{1}{2}\sqrt{(s''_{xx} - s''_{yy})^2 + 4(s''^2_{xy} + s''^2_{xz} + s''^2_{yz})} \right]^a$$
$$+ \left[\frac{3}{2}(s''_{xx} - s''_{yy}) - \frac{1}{2}\sqrt{(s''_{xx} - s''_{yy})^2 + 4(s''^2_{xy} + s''^2_{xz} + s''^2_{yz})} \right]^a .$$ (12)

Together with the eight anisotropy parameters, the exponent $a \geq 1$ defines the equivalent stress measure. With reference to the works of Hosford (1976), Barlat et al. (2003) recommend $a = 8$ for FCC materials.

The equivalent plastic strain rate is defined as work-conjugate to the equivalent stress, i.e.

$$\dot{\bar{\varepsilon}}_p := \frac{\boldsymbol{\sigma} : \dot{\boldsymbol{\varepsilon}}_p}{\bar{\sigma}}$$ (13)

5.2. Anisotropic fracture criterion

The anisotropic nature of the observed fracture response is described using the fracture initiation model proposed by Luo et al. (2012). The heart of Luo's model is an anisotropic equivalent strain definition which takes the value 0 in the material's original state and evolves according to

28

$$\dot{\bar{\varepsilon}}_f = \sqrt{\frac{2}{3}\left(\boldsymbol{\beta}\dot{\vec{\varepsilon}}_p\right)\cdot\left(\boldsymbol{\beta}\dot{\vec{\varepsilon}}_p\right)}, \tag{14}$$

Where $\vec{\varepsilon}_p$ is the vector of the components of the plastic strain in the material basis, $\vec{\varepsilon}_p = (\varepsilon_{11}^p, \varepsilon_{22}^p, \varepsilon_{33}^p, \sqrt{2}\varepsilon_{12}^p, \sqrt{2}\varepsilon_{13}^p, \sqrt{2}\varepsilon_{23}^p)$, with the first axis along the rolling direction and the second along the transverse direction. As proposed by Luo et al. (2012), we assume a strain transformation matrix of diagonal form:

$$\boldsymbol{\beta} = \begin{bmatrix} 1 & 0 & 0 & 0 & 0 & 0 \\ 0 & \beta_{22} & 0 & 0 & 0 & 0 \\ 0 & 0 & \beta_{33} & 0 & 0 & 0 \\ 0 & 0 & 0 & \beta_{12} & 0 & 0 \\ 0 & 0 & 0 & 0 & 1 & 0 \\ 0 & 0 & 0 & 0 & 0 & 1 \end{bmatrix}. \tag{15}$$

Due to the absence of experimental data for different stress states, we used the stress state independent version of Luo's model. In other words, fracture is assumed to initiate when $\bar{\varepsilon}_f$ reaches a critical value $\bar{\varepsilon}_f^*$. The resulting anisotropic fracture criterion therefore features four parameters $\{\beta_{22}, \beta_{33}, \beta_{12}, \varepsilon_f^*\}$ that need to be identified from experiments.

29

6. Simulations

6.1.Plasticity model parameter identification

The parameters defining the equivalent stress measure $\{\alpha_1, \alpha_2, ..., \alpha_8\}$ are identified from the tension experiments performed at a constant strain rate of $1.8 \times 10^{-4} / s$. In particular, we base our calibration on six independent measurements (Tab. 2) extracted from the uniaxial tension experiments: the flow stress values $\{Y_0, Y_{45}, Y_{90}\}$ at an axial strain of 0.002 in the different specimen orientations, and the corresponding Lankford ratios $\{r_0, r_{45}, r_{90}\}$. In addition, the plane strain tension flow stresses $\{Y_{45}^{PS}, Y_{90}^{PS}\}$ as estimated from the results of notched tension experiments (NT06) along the diagonal and transverse direction are used. In these experiments, plane strain tension conditions dominate only when well into the plastic regime. As a consequence the ratio of peak average stresses in those experiments to peak stress in the reference test (uniaxial tension in rolling direction) is used to deduce $\{Y_{45}^{PS}, Y_{90}^{PS}\}$.
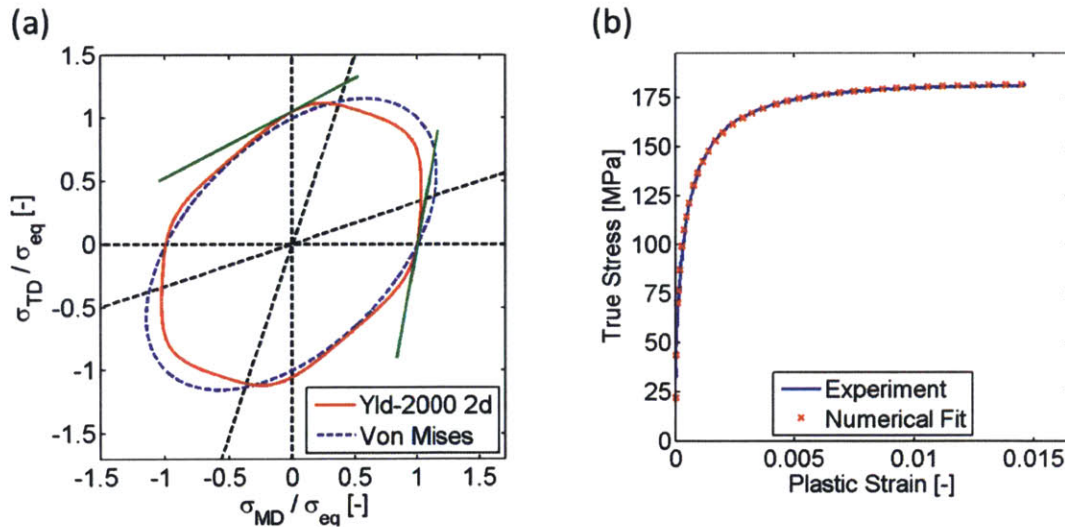

Figure 10. (a) Visualization of flow potential in stress space, assuming zero shear stress in the material basis; (b) Equivalent stress versus equivalent plastic strain curves for uniaxial tension at a strain rate of 1.8×10-4/s

It is straightforward to derive analytical expressions of the flow stresses and Lankford ratio's based on our proposed constitutive model. As a result, the non-linear relationship between the theoretical estimates of the eight experimental measurements $\{\tilde{Y}_0, \tilde{Y}_{45}, \tilde{Y}_{90}, \tilde{r}_0, \tilde{r}_{45}, \tilde{r}_{90}, \tilde{Y}_{45}^{ps}, \tilde{Y}_{90}^{ps}\}$ and the parameters $\{\alpha_1, \alpha_2, ..., \alpha_8\}$ is obtained. The $\{\alpha_i\}$ are consequently determined using a downhill simplex algorithm to minimize the error between the theoretical estimates and the experimental results (Tab. 3). A plot of the flow potential defined by the equivalent stress measures is shown in Fig. 10a for normal stress loading along rolling and transverse directions. The comparison with the isotropic quadratic von Mises potential highlights the effects of anisotropy and of the non-quadratic formulation. Note that the slopes of the tangents (green lines) at the intersection points with the coordinate axes visualize the constraints imposed by the Lankford ratios r_0 and r_{90}.

Testing Direction	Rolling ($\theta = 0$)	Diagonal ($\theta = 45$)	Transverse ($\theta = 90$)
Y_θ [MPa]	166*	162*	177*
r_θ [$-$]	0.2*	1.5*	1.1*
Y_θ^{UTS} [MPa]	182	180	191
ε_U [$-$]	0.018	0.020	0.017
ε_T [$-$]	0.023	0.034	0.023
Y_θ^{ps} [MPa]	168	176*	180*

Table 2. Material properties determined from uniaxial tension testing at a reference strain rate of $\dot{\varepsilon}_0 = 1.8 \times 10\%^{-4}/s$, at different angles with respect to the rolling directions: yield strength Y_θ (0.2% rule), Lankford ratio r_θ, ultimate strength Y_θ^{UTS}, engineering strain at ultimate strength ε_U, engineering strain to fracture ε_T. Material properties deduced from notched tension experiments: plane strain yield strength Y_θ^{ps}.

* used for equivalent stress calibration.

The function $k[\bar{\varepsilon}_p]$ is identified from the stress-strain response in a uniaxial tension experiment performed at a constant strain rate of $1.8 \times 10^{-4} / s$. To facilitate the calibration, we therefore chose the reference strain rate $\dot{\varepsilon}_0 = 1.8 \times 10^{-4} / s$, i.e. the measured uniaxial stress versus plastic strain curve corresponds to the equivalent stress versus equivalent plastic strain curve (Fig. 9). This curve is then approximated through the parametric form

$$k[\bar{\varepsilon}_p] = Y + Q(1 - \exp[-b\sqrt{\bar{\varepsilon}_p}]) .\qquad (16)$$

with the strain hardening parameters $\{Y,Q,b\}$ (Tab. 3).

The relative viscosity function f_v is identified from the uniaxial relaxation experiment (along the rolling direction for which $\bar{\sigma} = |\sigma|$). During the relaxation phase, the total strain rate is approximately zero,

$$\frac{\dot{\sigma}}{E} + \dot{\varepsilon}_p \cong 0 .\qquad (17)$$

and the viscoplastic constraint reads

$$\ln\left[\frac{\bar{\sigma}}{k[\bar{\varepsilon}_p]}\right] = f_v\left[\ln\left[-\frac{\dot{\sigma}}{E\dot{\varepsilon}_o}\right]\right] .\qquad (18)$$

The superposing blue curves in Figure 6d present the experimental results obtained from eight relaxation phases out of a total of three different relaxations experiments. The red dots show a third-order polynomial fit to the experimental data which is also taken as parametric form of f_v in the subsequent numerical simulations. A linear fit yields a strain rate sensitivity of about $m \cong 0.027$.

α_1	α_2	α_3	α_4	α_5	α_6	α_7	α_8	a	Y	Q	b
0.687	1.149	1.471	1.027	1.051	0.983	1.049	0.837	8	39	143	48

Table 3. Viscoplasticity model parameters.

6.2. Fracture model parameter identification

The fracture model parameters $\{\beta_{22}, \beta_{33}, \beta_{12}, \varepsilon_f^*\}$ are identified from the Hasek punch experiments for different material orientations. To determine the *instant of fracture initiation*, it is assumed that fracture initiates in the experiments when first cracks becomes visible in the DIC images (see representative picture shown in Fig. 9a). The strain fields were calculated using a 2D Gaussian kernel of half-width of about 50 microns. The *location of fracture initiation* is determined as the point of maximum strain at the instant of fracture initiation. Note that similar fracture strains have been identified when repeating the above procedure for different kernel sizes (100 and 200 microns).

The surface strain history at the identified location of fracture initiation was extracted and applied to a single-element simulation, using an algorithmic version of the proposed constitutive model implemented into the FE code Abaqus/Explicit using the VUMAT user material interface. This computation yields the history of the plastic strain components and the equivalent plastic strain, and their respective rates of change, at the assumed location of fracture initiation. The model parameters $\{\beta_{22}, \beta_{33}, \beta_{12}, \varepsilon_f^*\}$ (Tab. 4) are then obtained from a least-square fit of the anisotropic fracture model to the data from the nine HS experiments.

6.3. Finite element simulation of all notched tension experiments

Finite element simulations are performed of all tensile experiments. For each notched specimen, we discretized the region between the displacement measurement points (blue dots shown in Fig. 2) using an element size of about 40 microns near the specimen center. Zero normal displacement conditions are applied to the nodes that are located on the three orthogonal symmetry planes of the specimen. A representative mesh of an NT2 specimen is shown in Fig. 11b. Due to the absence of pronounced through-thickness necking prior to specimen fracture, only one element along the thickness direction turned out to be sufficient. We repeated selected simulations with four elements along the thickness direction and found nearly identical results. As compared to notched tension experiments on conventional sheet materials that fail at strains well above 0.5 (e.g. Dunand and Mohr,

2010), rather coarse meshes are acceptable here since the present aluminum foil failed already at strains of 0.05.

The experimentally measured axial loading velocity is applied to the top boundary of the FE mesh. The comparison of the solid and dotted lines in Fig. 5c demonstrates that the model is able to predict the dependency of flow stress on the strain rate. Simulations of the notched tension specimens for different notch radii and material orientations also show good predictions of the force-displacement relationship (Fig 12). Note that the circle symbols marking the end of all dotted curves in Fig. 12 correspond to the instant at which the anisotropic fracture criterion predicts fracture initiation. Fracture is accurately predicted for NT2 geometries for which the stress state is according to simulations, closest to that obtained in the Hasek punch experiments. However the predictions lose accuracy with increased notch acuity, which may be attributed to an effect of the stress state on fracture initiation.
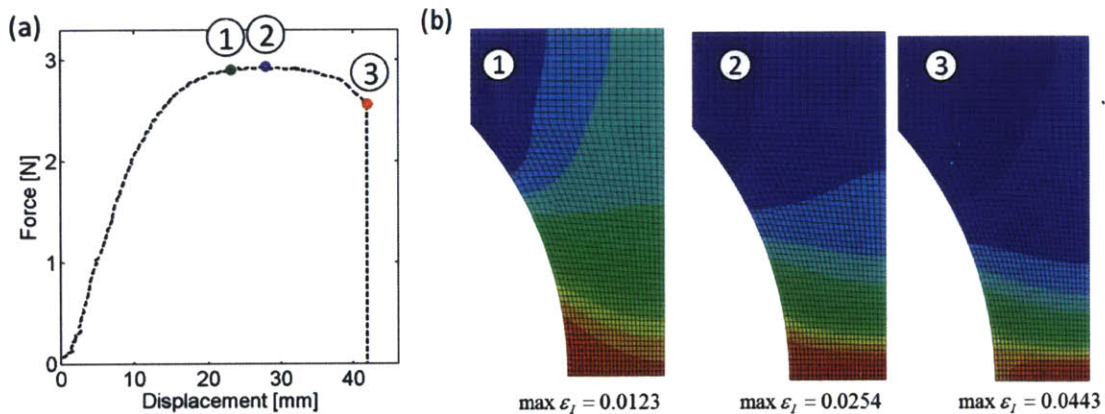

Figure 11 . FE analysis of an NT2-TD specimen: (a) force-displacement curve, and (b) selected contour plots of the maximum principal strain distribution.

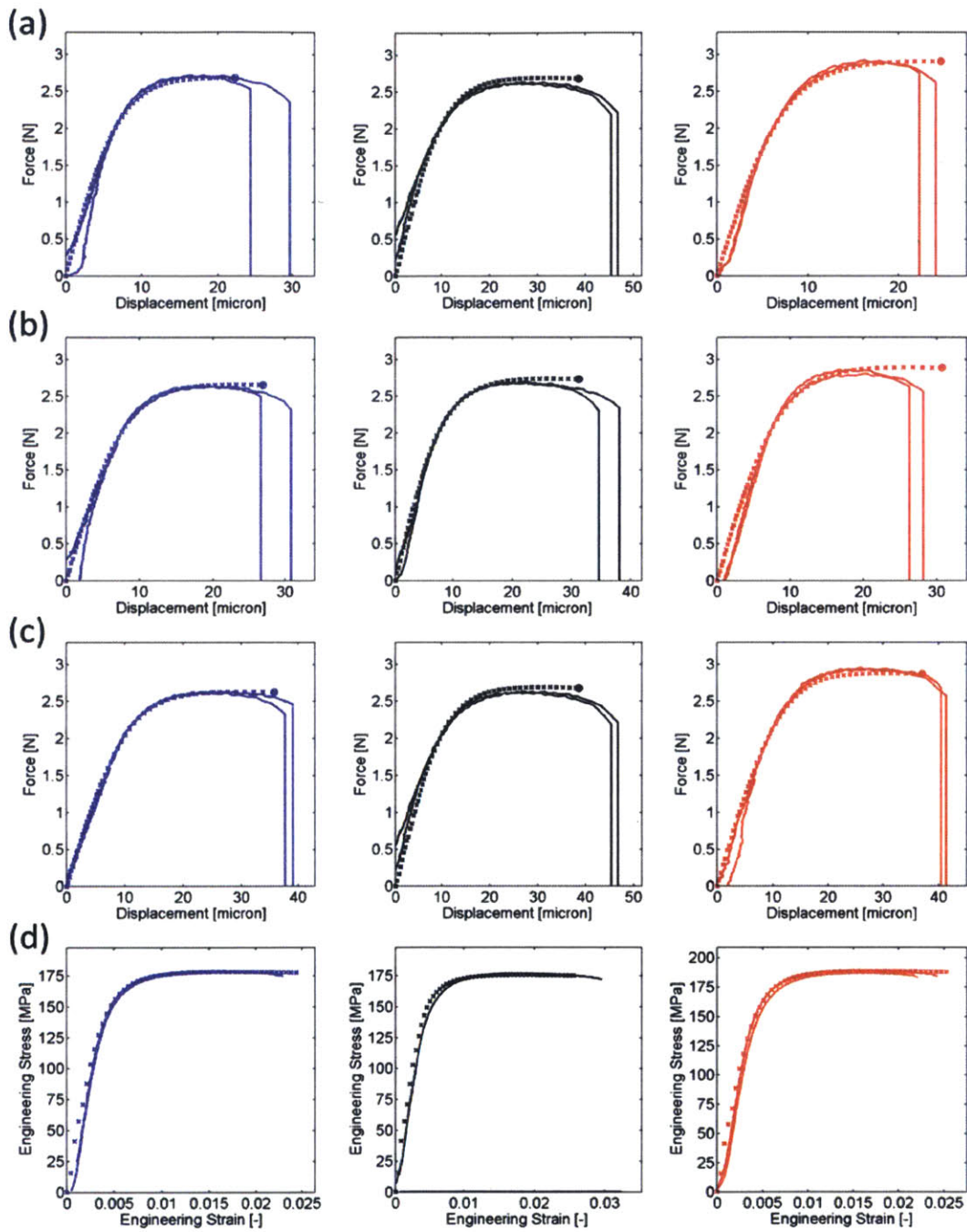| β_{22}	β_{33}	β_{12}	ε_f^*
1.04	1.48	0.31	0.047

Table 4. Fracture model parameters.

34

Figure 12. Comparison of simulation (solid dots) and experimental results (thin solid lines) for (a) NT06, (b) NT1, (c) NT2, and (d) UT.
For notched tension experiments, the end of each curve corresponds to the instant of fracture initiation (as measured or predicted by the model).

7. Conclusions

Aluminum alloy 1235-H18 foils are used as current collectors in Li-ion battery cells. In view of predicting the thermal runaway of batteries after accidental damage, the plastic and fracture response of this $16\mu m$ thick foil material is investigated experimentally. Tension experiments on dogbone-shaped and notched specimens are performed using a newly-developed micro-tensile testing device. In addition, Hasek fracture experiments are completed using a custom-made micro-punch testing device. The specimens with less than $1mm$ wide gage sections as well as the testing devices have been designed such that these can be conveniently inserted into an optical or scanning electron microscope. As a result, macroscopic strain fields with a resolution of about 10 microns could be determined based on microscopic images through digital image correlation.

It is found that the aluminum foil exhibits pronounced anisotropy with Lankford ratios ranging from 0.2 to 1.5. Furthermore, as expected for polycrystalline materials with submicron grain dimensions, the stress-strain response is highly strain rate sensitive even for relatively slow loading velocities. Within the range of strain rates tested here (10^{-5} to 10^{-2}), the average strain rate sensitivity is about $m \cong 0.027$. Based on our experimental observations, a new anisotropic viscoplasticity model is proposed combining a Barlat-type of flow potential with a non-linear relative viscosity function. The onset of fracture is predicted using a stress-state independent form of the anisotropic fracture initiation model of Luo et al. (2012). After calibrating the visco-plasticity model based on uniaxial tension and relaxation experiments, the anisotropic constitutive model for has been successfully validated based on a series of notched tension experiments with three different notch radii and three different specimen orientations.

References

Mikolajczak C., Kahn M., White K., Long R.T. (2011), Lithium-ion batteries hazard and use assessment. Fire Pro. Res. Found., 76 (90).

Wei Q. (2007), Strain rate effects in the ultrafine grain and nanocrystalline regimes - influence on some constitutive responses, J Mater Sci 42, 1709-1727

Hill R. (1948), A theory of the yielding and plastic flow of anisotropic metals, Proc. Roy. Soc., London A193, 281-297

Hershey A.V. (1954), The plasticity of an isotropic aggregate of anisotropic face centered cubic crystals, J. Appl. Mech. 21, 241-249

Hosford, W.F., 1972. A generalized isotropic yield criterion. J. Appl. Mech. Trans. ASME 39, 607-609.

Barlat, F., Brem, J.C., Yoon, J.W., Chung, K., Dick, R.E., Choi, S.H., Pourboghrat, F., Chu, E., Lege, D.J. (2003), Plane stress yield function for aluminum alloy sheets, Int. J. Plasticity 19, 1297.

Karafillis, A.P., Boyce, M.C., 1993. A general anisotropic yield criterion using bounds and a transformation weighting tensor. J. Mech. Phys. Solids 41, 1859-1886.

Bron, F., Besson, J., 2004. A yield function for anisotropic materials. Application to aluminum alloys. Int. J. Plasticity 20, 937-963.

Aretz, H., Hopperstad O.S., Lademo O.G. (2007), Yield function calibration for orthotropic sheet metals based on uniaxial and plane strain tensile tests, Journal of Materials Processing Technology 186, 221-235

Korkolis, Y.P., Kyriakides, S., 2008. Inflation and burst of aluminum tubes. Part II: An advanced yield function including deformation-induced anisotropy. Int.J. Plasticity 24, 1625-1637.

Dunand M., Maertens A.P., Luo M., Mohr D. (2012), Experiments and modeling of anisotropic aluminum extrusions under multi-axial loading - Part I: Plasticity, Int J. Plasticity 36, 34-49

May J., Höppel H.W., Göken M. (2005), Strain rate sensitivity of ultrafine-grained aluminium processed by severer plastic deformation, Scripta Materialia 53, 189-194

Dao M., Lu L., Asaro R.J., De Hosson J.T.M., Ma E. (2007), Toward a quantitative understanding of mechanical behavior of nanocrystalline metals, Acta Materiala 55, 4041-4065

Wei Y., Gao H. (2008), An elastic-viscoplastic model of deformation in nanocrystalline metals based on coupled mechanisms in grain boundaries and grain interiors, Materials Science and Engineering A 478, 16-25

Johnson, G.R., Cook, W.H., 1983. A constitutive model and data for metals subjected to large strains, high strain rates and high temperatures. In: 7th International Symposium on Ballistics, The Hague, pp. 541-547.

Roth C.C., Mohr D. (2014), Effect of strain rate on ductile fracture initiation in advanced high strength steel sheets: Experiments and modeling, Int. J. Plasticity 56, 19-44

Lin Y.C., Chen X.-M. (2011), A critical review of experimental results and constitutive descriptions for metals and alloys in hot working, Materials and Design 32, 1733-1759

Chaboche J.L. (2008), A review of some plasticity and viscoplasticity constitutive theories, Int. J. Plasticity 24, 1642-1693

Garofalo F. (1963),An Empirical Relation Defining the Stress Dependence of Minimum Creep Rate in Metals, Trans. of the AIME 227

Jonas J.J., Sellars C.M., McG. Tegart J. (1969), Strength and structure under hot-working conditions, Metall. Rev. 14, 1.

Brown S.B., Kim K.H., Anand L. (1989), An internal variable constitutive model for hot working of metals, Int. J. Plasticity 5, 95-130

Espinosa, H.D., Prorok, B.C., Fischer, M., 2003. A novel method for measuring elasticity, plasticity, and fracture of thin -films and MEMS materials. J. Mech. Phys. Solids 51, 47–67.

Xiang Y., Chen X., Vlassak J.J. (2005), Plane-strain bulge test for thin films, J. Mater. Res., Vol. 20, No. 9., 2360-2370.

Andre N, Coulombier M, De Longueville V, Fabregue D, Gets T, Gravier S, Pardoen T, Raskin J-P (2007), Microfrabication-based nanomechanical laboratory for testing the ductility of submicron aluminium films. Microelectronic Engineering 85, 2714-2718.

Gravier S, M Coulombier, A Safi, N André, A Boe, JP Raskin, T Pardoen (2009). New on-chip nanomechanical testing laboratory-applications to aluminum and polysilicon thin films. Journal of Microelectromechanical Systems18 (3), 555-569

Haque M.A., Saif M.T.A. (2003), A review of MEMS-based microscale and nanoscale tensile and bending, Experimental mechanics 43(3), 248-255.

Zhu, Y., & Espinosa, H. D. (2005), An electromechanical material testing system for in situ electron microscopy and applications, Proceedings of the National Academy of Sciences of the United States of America 102(41), 14503-14508.

Leisen, D., Rusanov, R., Rohlfing, F., Fuchs, T., Eberl, C., Riesch-Oppermann, H., & Kraft, O. (2015), Mechanical characterization between room temperature and 1000° C of SiC free-standing thin films by a novel high-temperature micro-tensile setup, Review of Scientific Instruments 86(5), 055104.

Gudlavalleti, S., Gearing, B. P., & Anand, L. (2005). Flexure-based micromechanical testing machines, Experimental mechanics, 45(5), 412-419.

Kim, J. S., & Huh, H. (2011), Evaluation of the material properties of an OFHC copper film at high strain rates using a micro-testing machine, Experimental mechanics, 51(6), 845-855.

Kachold, F. S., Lodes, M. A., Rosiwal, S. M., & Singer, R. F. (2013), Direct measurement of Young's modulus, fracture strength and fracture toughness of nanocrystalline diamond foil by means of tensile testing, Acta Materialia, 61(18), 7000-7008.

38

Hemker, K. J., & Sharpe Jr, W. N. (2007), Microscale characterization of mechanical properties, Annu. Rev. Mater. Res. 37, 93-126.

Gianola, D. S., & Eberl, C. (2009), Micro-and nanoscale tensile testing of materials, JOM 61(3), 24-35.

Berfield, T. A., Patel, J. K., Shimmin, R. G., Braun, P. V., Lambros, J., & Sottos, N. R. (2007), Micro-and nanoscale deformation measurement of surface and internal planes via digital image correlation, Experimental Mechanics, 47(1), 51-62.